LLNL-JRNL-2004658

Lawrence Livermore National Laboratory

Shock equation of state experiments in MgO up to 1.5 TPa and the effects of optical depth on temperature determination

R. Smith

September 2024

Disclaimer

This work performed under the auspices of the U.S. Department of Energy by Lawrence Livermore National Laboratory under Contract DE-AC52-07NA27344.

LLNL-JRNL-2004658

Lawrence Livermore National Laboratory

Shock equation of state experiments in MgO up to 1.5 TPa and the effects of optical depth on temperature determination

R Smith

May 2025

Disclaimer

This work performed under the auspices of the U.S. Department of Energy by Lawrence Livermore National Laboratory under Contract DE-AC52-07NA27344.

Shock equation of state experiments in MgO up to 1.5 TPa and the effects of optical depth on temperature determination

Zixuan Ye[1], Raymond F. Smith[2], Marius Millot[2], Melissa Sims[1], Dimitrios Tsapetis[3], Michael D. Shields[3], Saransh Singh[2], Anirudh Hari[1,4,5], June K. Wicks[6,*]

[1]*Department of Earth and Planetary Sciences Div. of Mechanical Engineering, Johns Hopkins University, Baltimore, MD 21218, USA*
[2]*Lawrence Livermore National Laboratory, Livermore, CA 94550, USA*
[3]*Department of Civil and Systems Engineering, Johns Hopkins University, Baltimore, MD 21218, USA*
[4]*Stanford University, Department of Materials Science and Engineering, and PULSE Institute, CA 94305, USA*
[5]*SLAC National Accelerator Laboratory, CA 94025, USA*
[6]*Department of Earth and Planetary Sciences, Johns Hopkins University, Baltimore, MD 21218, USA*

Laser-driven shock compression enables experimental study of phase transitions at unprecedented pressures and temperatures. One example is the shock Hugoniot of magnesium oxide (MgO), which crosses the B1-B2-liquid triple point at 400-600 GPa, 10,000-13,000 K (0.86-1.12 eV). MgO is a major component within the mantles of terrestrial planets and has long been a focus of high-pressure research. Here, we combine time-resolved velocimetry and pyrometry measurements with a decaying shock platform to obtain pressure-temperature data on MgO from 300-1500 GPa and 9,000-50,000 K. Pressure-temperature-density Hugoniot data are reported at 1500 GPa. These data represent the near-instantaneous response of an MgO [100] single crystal to shock compression. We report on a prominent temperature anomaly between 400 and 460 GPa, in general agreement with previous shock studies, and draw comparison with equation-of-state models. We provide a detailed analysis of the decaying shock compression platform including a treatment of pressure-dependent optical depth near the shock front. We show that, if the optical depth of the shocked material is larger than 1 μm, treating the shock front as an optically thick grey body will lead to a noticeable overestimation of the shock temperature.

I. Introduction

Understanding the structure and dynamics of planetary interiors requires a comprehensive knowledge of the phase diagram, equation-of-state (EOS), and transport properties of the main constituents at the relevant extremes of pressure (P) and temperature (T) ([1, 2]). Magnesium oxide (MgO), known as the mineral periclase, is expected to be a major component within the Earth's lower mantle due to the expected dissociation of Mg_2SiO_4 and $MgSiO_3$ with pressure ([3]), and may play a key role in planetary interior dynamics. While the ambient pressure NaCl-structure (B1 phase, $Fm\bar{3}m$ space group) of MgO is stable throughout the Earth's mantle ([4–7]), a transformation to the CsCl-structure (B2-phase, $Pm\bar{3}m$ space group) occurs between 400-600 GPa ([7, 8]); pressures found within the lower mantles of large rocky exoplanets ([7, 9–12]). Theoretical studies have emphasized the importance of this phase transformation on exoplanetary interior conditions due to an associated significant change in rheological properties with the high-pressure B2 phase exhibiting an estimated one hundred times reduction in viscosity ([13, 14]).

A number of theoretical studies have focused on MgO's phase transformations up to 1 TPa (1 TPa = 1000 GPa = 10 million atmospheres) ([10–12, 15–23]). Overall, there is consensus for the prediction of a B1/B2 transition near 500 GPa at 300 K. However, there is a larger disagreement at higher temperature, where phonon anharmonicity is expected to expand the region of B1 stability ([12, 15]). At 9500 K, for example, recent studies report a B1→B2 onset pressure range between ~250-480 GPa ([10–12, 15–20, 22–24]) (see Ref. ([8]) for a review). There are also significant differences regarding the predicted P-T conditions for melting ([12, 17]). Such large discrepancies illustrate the sensitivity to the underlying physics models used and the need for experimental data to validate these differing theoretical and numerical approaches.

In this study, we employ nanosecond laser irradiation to determine the response of an MgO [100] single crystal to uniaxial shock loading over a wide range of pressures (360-1515 GPa) and temperatures (8,600-47,000 K); states which encompass the predicted B1, B2, and liquid phase regions of stability. Using a decaying shock experimental design, coupled with time- and space-resolved *in situ* velocimetry and pyrometry techniques, we make single shot measurements at the shock front, for a continuum of Hugoniot states. These data, which reveal the sub-nanosecond response of the crystal lattice to shock compression, are compared against EOS models for MgO. We discuss the effect of shock front

*Corresponding author
Email address: wicks@jhu.edu (June K. Wicks)

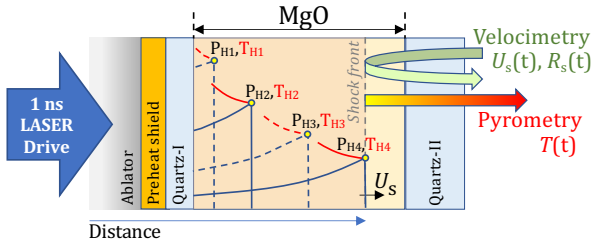

Figure 1. Experimental setup for uniaxial shock decay platform. A 1-ns high power laser pulse focused within an 800-μm spot uniaxially compresses the target assembly and produces a continuum of Hugoniot states, P_H-T_H, throughout the MgO sample. Due to pressure release states immediately behind the shock front the Hugoniot states accessed diminish as a function of shock propagation / distance. Four snapshots are illustrated with P_{H1}-T_{H1} > P_{H4}-T_{H4}. Behind the shock front the temperature increases due to adiabatic release from earlier-in-time higher P_H-T_H states (see Fig. 2 for details).

optical depth on temperature determinations in decaying shock experiments by investigating thermal emission and transmission of semi-transparent compressed MgO.

II. Shock Decay Experiments

To investigate the thermodynamic and optical properties of MgO shocked along the [100] direction, three decaying shock compression experiments were performed at the Omega-EP laser facility, located at the University of Rochester's Laboratory for Laser Energetics. The target design is shown in Fig. 1 and consists of a 20-μm thick diamond ablator, a 3-μm thick Au preheat shield and a ~300 μm thick MgO [100] single crystal bounded by two quartz layers which serve as standards for temperature determination (26) (see Table S1). The presence of the quartz layers is an improvement over previous designs and provides extra constraints on MgO pressure, reflectivity, and temperature determinations (27). The second quartz layer (Qtz-II) had an anti-reflection coating applied to the free surface to suppress optical back reflections from that interface.

The Omega-EP laser at 351-nm delivered up to 1250 J of laser energy in a 1-ns flat top pulse within an 800-μm diameter spot (using super-Gaussian distributed phase plates; see Fig. 5a) at the front surface of the diamond ablator. The resulting rapidly expanding plasma launched a temporally unsupported shock wave into the target package which uniaxially loaded the single crystal MgO along its [100] crystallographic axis. The Au preheat shield absorbs X-rays generated within the laser plasma which could otherwise prematurely heat

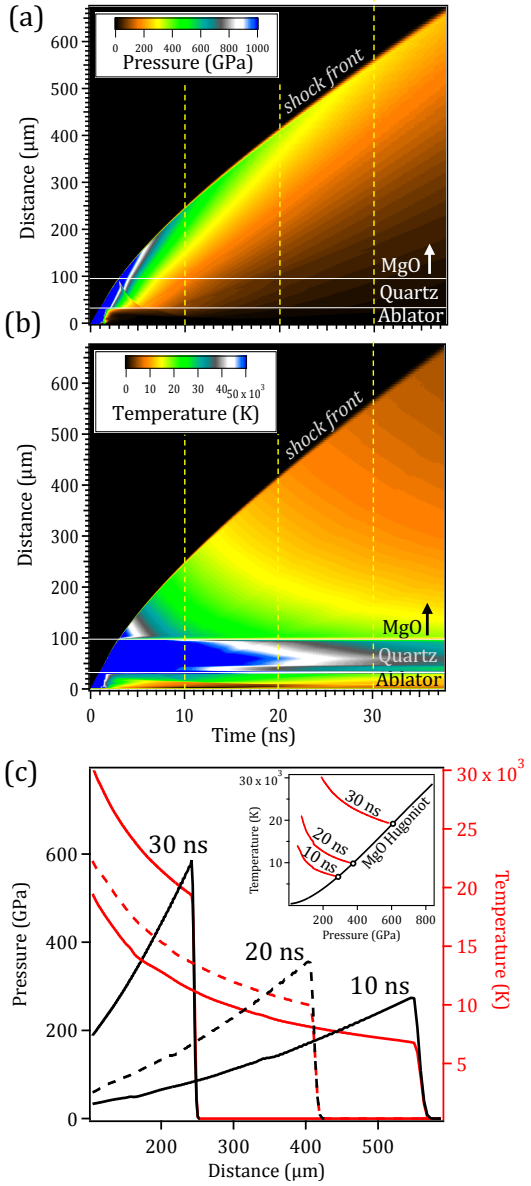

Figure 2. HYADES hydrocode simulations of shock decay platform. Lagrangian distance versus time map of **(a)** pressure and **(b)** temperature, for the experimental geometry illustrated in Fig. 1. **(c)** Distance lineouts of P and T at three different times (yellow dashed lines in (a) and (b)) illustrate how the pressure at the shock front decreasing in time. Temperature is observed to increase as a function of distance behind the shock front due to isentropic release from higher pressure (higher temperature) earlier-in-time shock states. The inset figure shows the T-P profiles taken behind the shock front at 10, 20 and 30 ns after the laser turns on. As the Sesame #7460 EOS used in the simulations only describes the B1 phase of MgO (25), there are no P-T slope changes which would be expected in the presence of a phase transformation.

the MgO prior to compression, and minimizes the potential for X-ray induced photoionization of the sample and/or the quartz plates which could render them partially opaque. The decaying shock wave weakens in amplitude as it propagates, providing access to a broad range of shock states within a single experiment. The optimized design ensured that the shock front pressure in MgO would reach the desired range (~300-1500 GPa) while being unaffected by reverberation waves that originated from previous layers. A detailed description of the multi-layer target is outlined in the Supplementary Materials and Table S1.

The experiments were designed with the aid of one-dimensional HYADES hydrocode simulations (28) which were used to calculate the hydrodynamic flow of pressure waves through the target assembly in time and space. Figures 2a and b shows the calculated pressure and temperature maps as a function of Lagrangian distance and time at, and behind, the shock front for the target and laser geometry in Fig. 1, where the color scale illustrates the magnitude of the calculated P-T states throughout the multilayer sample. To quantify the evolution of states, three distance lineouts of pressure and temperature are plotted in Fig. 2c, taken at 10, 20 and 30 ns after the 1-ns laser pulse turns on. The short laser pulse duration produces shock states which are unsupported in time. As the shock front propagates through the MgO sample the Hugoniot P-T states accessed, at this front, diminish due to the presence of release waves. At distances behind the shock front while pressure decreases, temperature is observed to increase.

In our decaying shock experiments, each "slice" of the sample is shocked from ambient, and subsequently - over sub-nanosecond timescales - experiences an adiabatic decompression. The higher the initial P_H-T_H state the hotter the release path, with $T_{Release}(t) < T_H$. Therefore, at any given time, there is a history of higher P_H-T_H states and associated hotter release paths (earlier times/propagation distances). The calculated temperature increase behind the shock front is due to a contribution from a continuum of progressively higher T release paths (see Fig. 2c).

In decaying shock experiments, if the shock front is optically thick (strongly absorbing to optical photons) and reflective we can obtain a collection of temperature vs shock velocity measurements. Streaked optical pyrometry (SOP; 590-850 nm bandwidth) (31) and velocity interferometry (VISAR: velocity interferometer system for any reflector; 532 nm probe wavelength) (29, 34) are employed to probe the shock-front and provide continuous measurements of spectral radiance (SOP), shock

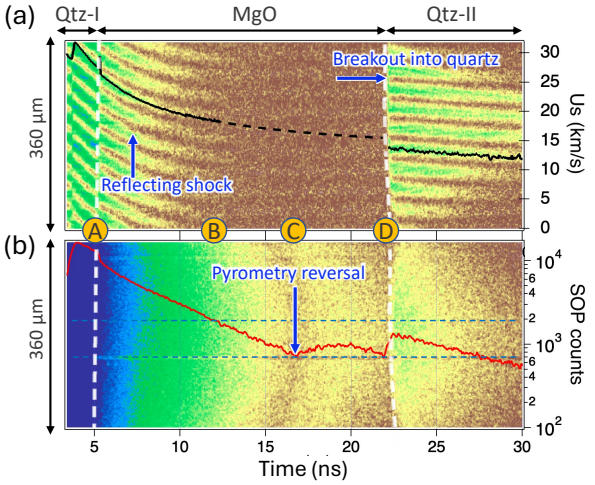

Figure 3. Shock decay velocimetry and pyrometry data. **(a)** Line-imaging VISAR interferogram (29, 30) in which shock front reflectivity enables accurate measurement of shock velocity (U_s) as a function of time (black solid curve). Events are labeled as A to D: After crossing the Quartz-I, the shock enters the MgO at A. VISAR directly tracks the decay in shock velocity (fringe shift) and in reflectivity (fringe amplitude) until B where the reflectivity is too low (below ~1%, see Fig. 4). For later times a model was employed to estimate U_s(t) (dashed black curve, see text for details) **(b)** Raw streaked optical pyrometer (SOP) data (31). The solid red curve represents the counts averaged over ~40 μm (taken between the two horizontal dashed blue lines). From point A the SOP initially records a smooth, exponential decay in spectral radiance as function of decreasing U_s, that we interpret as thermal emission. At C, the pyrometry signal reverses abruptly and rises before decreasing again. At D the shock enters the Quartz-II and a strong VISAR signal is recovered, together with a monotonous decay of the SOP.

velocity (U_s) (VISAR), and reflectivity (R) (VISAR) as a function of time. However, as discussed in Sec. IV, the extent to which the SOP is diagnosing the temperature of the shock front is dependent on the optical depth. More details on the experimental measurements and data analysis can be found in the Supplementary Materials and Ref. (26).

II.A. Shock Velocity Measurements

Figure 3a shows an example VISAR image for the decaying shock experiments. Analyzing the VISAR record reveals that, as the decaying shock transits the MgO layer, the shock velocity (U_s) decreases rapidly (the fringe phase is varying rapidly with time). In addition, the fringe amplitude rapidly decreases, which reveals that the shock front reflectivity is decreasing. At early times the shock compressed material (which is initially a transparent insulator) becomes electrically con-

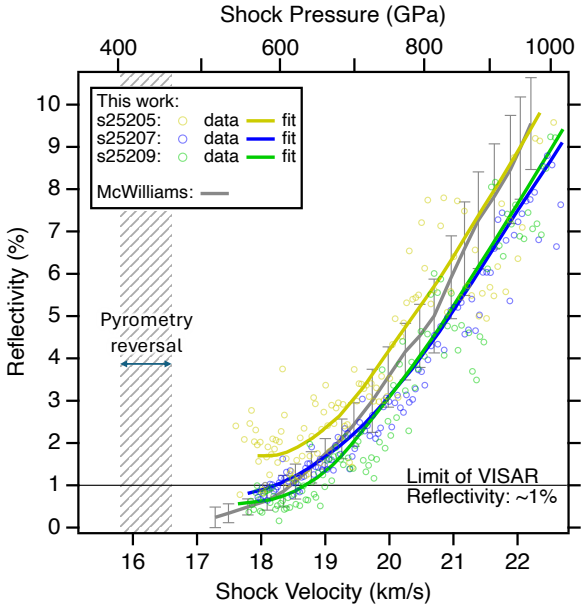

Figure 4. Shock front reflectivity measurements. The circles represent shock front reflectivity from VISAR amplitude analysis of the three decaying shock experiments, as a function of U_s. Shock pressure (top axis) is determined from a fit to previous Hugoniot data and the Rankine-Hugoniot equations (32) which relate U_s and P (Fig. 6). The corresponding solid curves represent smoothed data using Loess function for each shot. The VISAR is limited in measuring reflectivity below 1% (black dotted line), which corresponds to U_s~18 km/s for shots s25207 and s25209, consistent with values reported by McWilliams *et al.* (grey curve) (9). The estimated reflectivity for shot s25205 is systematically high possibly due to a non-ideal anti-reflection coating on the Qtz-II free-surface for that sample. A direct measurement of U_s range associated with the observed pyrometry reversal in Fig. 3b is not possible and so an extrapolation of the measureable U_s data was used (see text for details).

ducting so that the shock front becomes a good quality mirror. VISAR then directly tracks the shock front velocity. The optical depth of the compressed material is << 1 μm so that it is appropriate to assume that the radiance collected by the SOP is emitted by the shocked material right behind the shock front. The shock front in MgO becomes non-reflective below a U_s~18 km/s (event B in Fig. 3), below which the shock velocity in MgO cannot be inferred from the fringe phase analysis. Measured shock front reflectivity at the 532-nm VISAR wavelength is shown in Fig. 4 as a function of U_s and P. The VISAR signal is retrieved again once the shock enters the quartz-II window (event D in Fig. 3) where, above shock pressures of ~100 GPa, a reflecting silica liquid is generated (35).

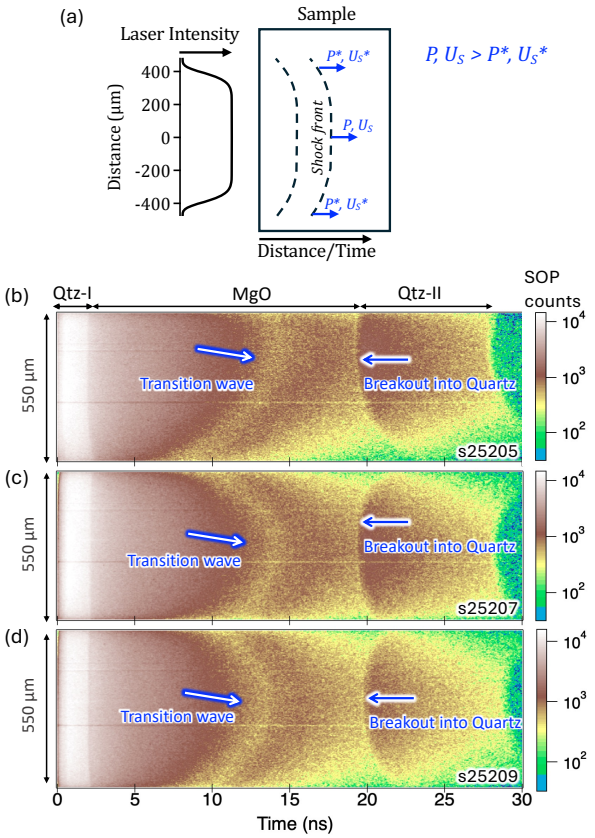

Figure 5. Summary of raw SOP images. **(a)** The laser focal spot spatial profile produces lower P-U_S states at the edge of laser drive. The SOP images for shots **(b)** s25205, **(c)** s25207, and **(d)** s25209 are displayed with a spatial field of view of ~550 μm. The magnitude of thermal emission detected by SOP is denoted by color in a logarithmic scale, as shown on the right side for each shot. The spatial planarity of the drive laser, which has lower intensity at the edges compared to the center, characterizes the curvatures of the transition wave, and the breakout wave into quartz-II. The breakout wave into quartz-II exhibits a rightward concave curvature, indicating that the shock wave travels slower at the edges. In contrast, the transition wave observed in each shot displays a leftward concave curvature. This is attributed to the lower pressures attained at the edges of the drive, which enable the transition condition to be reached earlier (33).

Even though U_s in MgO is not directly measurable < ~18 km/s, estimates of U_s below this value are desirable to for determining the Hugoniot pressures associated with the SOP thermal emission. To extrapolate U_s(t) in MgO over this non-reflective period (dashed line in Fig. 3b), previous studies assume that shock velocity decays double-exponentially and that phase transitions have little effect on the decay rate (9, 26, 36–38). In this study, the decay rate was constrained by

fitting the shock velocity as a function of time from hydrocode simulations (Fig. 2). An additional constraint is the calculated U_s in MgO just before the shock enters the quartz-II layer (moment D in Fig. 3). Uncertainty in this extrapolation was determined with the aid of UQpy formalism (39) (see Sec. S3 for details).

II.B. Measurements of thermal emission

Figure 3b shows an example SOP image for the decaying shock experiments, taken over a 360 μm field of view, where the shock front is found to be sufficiently planar that it is meaningful to average the SOP counts versus time to extract a SOP vs time lineout. Here we assume that: (1) the detected spectral radiance is from thermal emission, (2) the shocked MgO radiates as a grey body and, (3) the shock front is optically thick. With these assumptions MgO shock temperature was determined from the measured SOP counts. The details of the analysis are described in Ref. (26) and Supplementary Materials.

In addition to the quantitative analysis of the central region of the shock, taking advantage of the 1D imaging capacity of the SOP enables us to obtain additional information to strengthen our interpretation of the VISAR and SOP data. SOP images for all three experiments, over a 550 μm field of view, are shown in Fig. 5. Figure 5a shows the average spatial distribution of the laser focal spot, where 95% of the laser energy is constrained with a diameter of 819 μm. The spatial profile of the pressure imparted into the diamond ablator is assumed to approximate the laser intensity distribution (40). During shock propagation within the sample the spatial extent of the uniform central region is eroded by lateral pressure release from the edge of the drive. In the decaying shock geometry, where the shock front pressure decreases in time, the lower pressure wings on the drive result in phase transformations occurring earlier in time, giving rise to a distinct left facing concave curvature to associated with the "transition" wave. In the absence of a phase transition the lower pressure wings of the drive, which have an associated lower U_S, arrive at interfaces in the sample later in time. This gives rise to the right facing concave curvature of the "breakout into quartz" feature. For all pressure and temperature estimates, only VISAR and SOP data at the spatial center of the drive was considered.

III. Results

III.A. Pressure-density-temperature Hugoniot data

As the shock front transits from the Qtz-I layer to MgO (moment A in Fig. 3a), to ensure the continuity of pressure and particle velocity at that interface, a second shock, i.e., a reshock, is launched backwards into the quartz plate. The transmitted shock must, therefore, satisfy the Rankine-Hugoniot equations for a single shock in MgO and for the reshock state in quartz (41).

Using the measured U_s(t) in Qtz-I and MgO just before and after moment A in Fig. 3a, an impedance matching analysis (42) was conducted with the known EOS of the quartz standard (26, 43–45) used to determine the MgO Hugoniot pressure and density (ρ) at ~1500 GPa. For the quartz Hugoniot, we use the fit reported by Fernandez-Pañella *et al.* (46). The quartz reshock curve is modeled as a Mie-Grüneisen correction to the reflected Hugoniot, with a constant Grüneisen parameter, $\gamma = 0.64 \pm 0.05$, following Hicks *et al.* (43). Systematic uncertainties from the model and random uncertainties from the measurements are propagated with a Monte-Carlo algorithm (26).

The data for three shots, shown in Fig. 6 as the red diamond symbols, represent 2.5-fold compression, and are found to be in agreement with the Sesame #7460 EOS table for MgO (25) (see also Figs. S2, S3). The temperature data at moment A in Fig. 3, calculated from SOP to be ~47,000 K, are shown in the inset of Fig. 6 and are consistent with the data from McCoy *et al.* (47).

III.B. Shock decay determination of T-P states

Since we are tracking the shock front, we can use the Rankine Hugoniot equations and the previously determined U_s-u_p relationship (Fig. S2) to infer the pressure time history P(t) from the measured U_s(t) profile. In our experiments, the sample is uniaxially-compressed. While the use of the term "pressure" throughout the paper suggests a hydrostatically-compressed state, we cannot rule out the presence of deviatoric stresses which would, in the case of our measurements, and all previous Hugoniot measurements (5, 9, 10, 16, 48, 50), give rise to higher values of longitudinal stress and therefore reported pressure. In the analysis of Fowles (51) using the Lévy-von Mises yield criterion (52) this stress deviation corresponds to two-thirds the yield strength. However, the high-pressure strength of MgO is unknown. In Fig. 7, P-T data from our three shock decay experiments are represented by the green, blue, and orange curves. Between 400

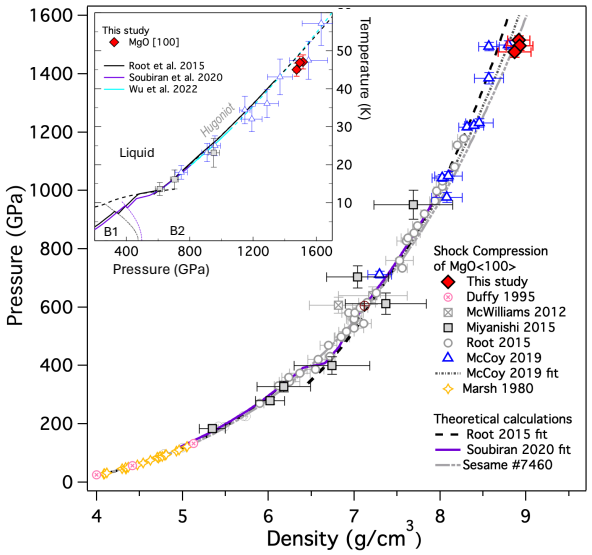

Figure 6. Hugoniot P-T-ρ data. Our pressure-density (P-ρ) data (red diamonds) from impedance matching analysis are compared with previous published shock compression data (open symbols) (5, 9, 10, 16, 47, 48). Theoretical calculations are shown as dashed black, solid purple, and gray dashed-dot-dot-dot curves (10, 12, 25). The SESAME EOS table #7460 (25) best describes our P-ρ data at 1500 GPa. The inset figure shows temperature data for liquid MgO as a function of pressure. Our temperature measurements are consistent with Hugoniot models from Wu *et al.* (49), Root *et al.* (10), and Soubiran *et al.* (12). A summary of the MgO *P-T-*ρ data may be found in Table S2.

GPa and 460 GPa (between points A and B), we observe a clear temperature anomaly along the MgO shock Hugoniot at similar *P-T* conditions reported from previous shock decay studies (9, 36) (see Fig. 8). Also shown are shock temperature data (measured with the same pyrometry instrument) during steady shock experiments aimed at documenting the atomic structure with in-situ nanosecond X-ray diffraction (open square symbols, color coded to reflect the measured crystalline phase within the bulk) (8). Our data is plotted alongside EOS models for the B1-B2 phase boundary (10, 12, 23), the melt line (6, 10, 12), and the Hugoniot (6, 12).

IV. Discussion

In the absence of a phase transformation, shock compressed materials become hotter and the rate of increase of temperature with increasing shock pressure is usually varying slowly. When an MgO sample undergoes a phase transformation under shock compression pronounced changes in *P-T* slope are predicted. The calculated Hugoniot for MgO based on an equilibrium EOS model such as the one from Soubiran *et al.* (12) which incorporates the B1, B2 and liquid phases of MgO (solid blue curve in Fig. 7) predicts several *P-T* slope changes to be detectable with the shock decay platform: (i) B1-B2 coexistence, (ii) B2-liquid coexistence, and (iii) a pure liquid *P-T* slope that is markedly shallower than the near identical *P-T* slopes within the B1 and B2 phases (12).

Our data reveal a reproducible shock temperature vs U_s/pressure, with a dramatic temperature reversal near 15.8 km/s and 400 GPa (Fig. 7). Such a reversal is qualitatively identical to the prediction from Soubiran *et al.* (12). However, the extent of the observed temperature reversal and the absence of other expected slope changes are hard to reconcile.

Two previous decaying shock studies on MgO [100] which measured radiance vs U_s, from which T-U_s and T-P was determined (9, 36), also observed a large temperature reversal between ~400-500 GPa, in general agreement with our data (see Fig. 8). While this observed temperature excursion has several possible interpretations: B1→B2 transition, B2→melt transition, or B1→melt transition, McWilliams *et al.* (9) interpreted this feature as being due to the B1-B2 transition, whereas Bolis *et al.* (36) attributed it to the B2-melt transition. In addition, while McWilliams *et al.* (9) reported a slight change in the slope in T-U_s plane at ~13,000 K, and a corresponding pressure of ~600 GPa, which they assigned to the B2-melt transition, this was not observed in this study, nor was it reported in the shock decay study of Bolis *et al.* (36).

A full interpretation of our shock decay data on MgO [100], presented in Fig. 7, will likely require exploring behavior along different orientations within the MgO crystal (Ye *et al.*, in preparation (53)), and is beyond the scope of this paper. We note that equilibrium EOS models do not capture time-dependent deformation effects or potential orientation-dependent deformation associated with uniaxial compression along different crystallographic directions in the MgO. These effects may contribute to the differences between our data and the predictions of EOS models and should be the focus of continued research.

In order to try to reconcile our measurements with the expected T vs U_s from the most advanced numerical simulation methods, we investigated how the assumption that the material behind the shock front behaves as an optically thick grey body affect the data analysis and interpretation. For the SOP determination of shock temperature, thermal emission is collected from an ex-

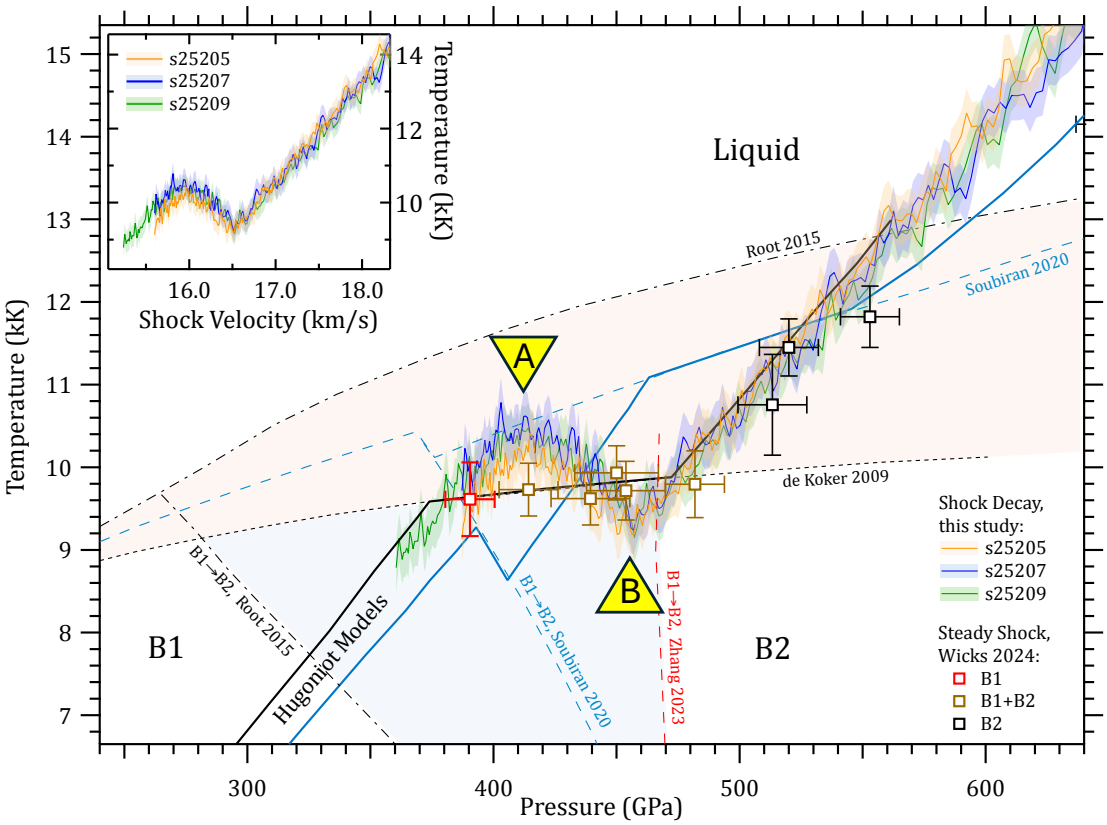

Figure 7. Shock temperature data and predicted phase boundaries. Phase map of MgO with the stability fields for the B1, B2 and liquid phases shown. Bounding predictions for the *P-T* onset of the B1–B2 (shaded blue region (10, 12, 23)) and the onset of melt (shaded orange region (6, 10, 12)) are shown (see Ref. (8) for a full review). Our decaying shock *P-T* data are presented as the orange, blue, and green curves and exhibits a large temperature excursion between 400 and 460 GPa (between points A and B). Two different Hugoniot models are shown: the B1-B2-liquid Hugoniot from Soubiran *et al.* (12) (blue curve), and the B1-liquid Hugoniot from de Koker *et al.* (6) (black curve). Also shown are the X-ray diffraction (XRD) + steady shock data from Wicks *et al.* (8) (open square symbols) which represent shock front temperatures, and bulk determinations of structure. The inset shows our data in T-U_s space. We see a strong temperature reversal between U_s~15.8-16.6 km/s, which is very repeatable over the three shots. There is no signature of a T-U_s slope change near 13 kK as was reported in Ref. (9).

tended volume which encompasses the shock front and pressure states behind the shock front. This volume is defined by the optical depth. The values reported in the recent work by Wicks *et al.* (8) (Fig. 9) are significantly higher than values assumed in shock decay studies of MgO (9, 36). As discussed below, when interpreting shock decay temperature data, it's important to understand the effect optical depth has on the calculated temperature.

IV.A. Optical depth effect on shock front temperature measurements

In the determination of temperature from SOP, gray-body emission is assumed, where emissivity is defined as ϵ(t)=1-R(t), with shock front reflectivity R(t) determined from VISAR measurements (31). This approach assumes that the region immediately behind the shock front is optically thick, which is considered a good approximation for reflecting shock fronts. However, as indicated in VISAR data in Fig. 3a and the extracted reflectivity data in Fig. 4, MgO shock front reflectivity decreases rapidly below 600 GPa which suggests that the optical depth may be significant at lower pressures and should be explicitly considered for accurate temperature determination.

The optical depth of MgO along the shock Hugoniot was recently measured by Wicks *et al.* (8) between 397 GPa and 635 GPa, where it was found to increase exponentially with decreasing pressure and exceeds 10 μm at 397 GPa (see Fig. 9) – significantly higher than previously assumed (9, 36). This indicates that the thermal emission detected by SOP originates from an extended

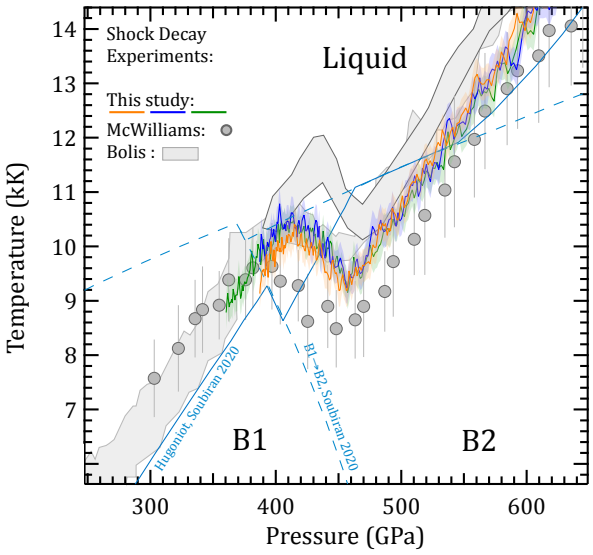

Figure 8. Our shock decay data on MgO [100] compared to previous studies (9, 36). Also plotted are the Hugoniot and B1-B2-liquid phase boundaries predicted by the calculations of Soubiran *et al.* (12). As described in Ref. (8) the decaying shock data of McWilliams *et al* (9) has been corrected in pressure based on the subsequent U_s-u_p measurements by Root *et al*. (10).

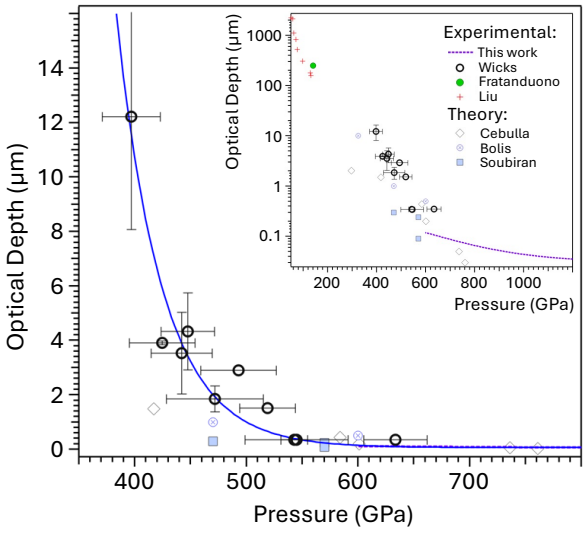

Figure 9. Optical depth as a function of shock pressure. The optical depth of MgO is calculated from VISAR reflectivity measurements (dotted purple curve) above 600 GPa (see Sec. S6). Also plotted are optical depth measurements in steady shock experiments from Wicks *et al.* (8) (open black circles). Calculations from Cebulla *et al.* (54), Bolis *et al.* (36), and Soubiran *et al.* (15) are plotted as diamonds, cross circles, and squares for comparison. The solid blue curve fits the solid data from Wicks *et al.* (8) and the liquid data from this study. The expanded plot on the inset shows data from Liu *et al.* (55) and Frataduono *et al.* (50).

volume behind the shock front, where temperature profiles are complicated by rarefaction and phase transformation waves. Here we describe an emission model for partially-transparent MgO, to determine the effect of optical depth on the temperature measurements in shock decay experiments.

At any given time, the measured SOP signal represents an integration of the thermal emission from temperature gradients (behind the shock front, as in Fig. 2c) transmitted through compressed MgO with a pressure/thickness dependent optical depth. The optical transparency of a shocked volume depends on the density of scattering centers which proliferate due to irreversible microstructural refinement under compression (e.g., due to dislocation mediated plasticity and/or a phase transformation) (56). We therefore assume within our model, that the shock pressure-dependent optical depth reported by Wicks *et al.* (8) (Fig. 9), is constant throughout the release states behind the shock front.

To estimate the effect of optical depth on shock-decay temperature measurements, we use the *P-T* Hugoniot predictions of Soubiran *et al.* (12) (purple curve in Fig. 10) as a test case input to a model which accounts for optical depth versus pressure (Fig. 9). Our model simulates how the experimentally-determined $P-T$ values in shock decay experiments are altered (over actual shock-front $P-T$ values) by integrating thermal emission over extended regions behind the shock front.

We first estimate the isentropic release paths from the Hugoniot states (dashed lines in Fig. 10a), including temperature changes at the B1, B2, and liquid phase boundaries, to model the temperature distribution and corresponding thermal emission behind the shock front as a function of time as the shock propagates (see Supplementary Material Section S6 for details). By combining the calculated pressure distribution shown in Fig. 2c with the estimated release isentropes shown in Fig. 10a, the SOP-detected thermal emission at the shock front is simulated. This simulation represents a volume-integrated and optical-depth dependent contribution from states behind the shock front. As large optical depth values result in measured emission from hotter regions behind the shock front, the apparent temperature will always be hotter than the actual shock front temperature. This effect is more pronounced for lower

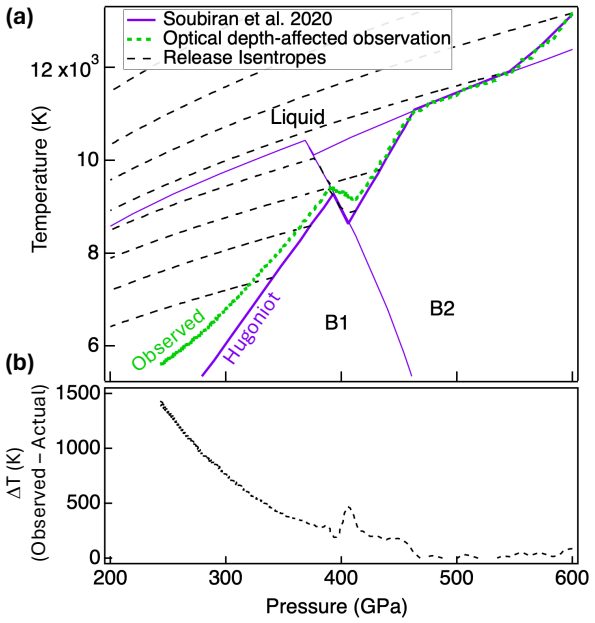

Figure 10. Optical depth effects on simulated temperature measurements along Soubiran Hugoniot path. **(a)** The calculated Hugoniot and B1-B2-liquid phase boundaries from Soubiran *et al.* (12) are plotted as bold and light purple curves, respectively. The release isentropes (black dashed) are extrapolated from the single-phase Sesame EOS table #7460 (25) and have an imposed shift to a higher temperature (~650 K) when crossing the B1-B2 boundary. An optical-depth dependent model shows that the apparent shock front temperatures (green dotted) present higher values than the actual temperatures (bold purple) and flattens out the temperature excursion from the B1-B2 phase transition. **(b)** The temperature difference between the simulated experimental measurements (observed) versus the actual Hugoniot curve.

shock pressures where optical depth increases (Fig. 9).

A comparison of the apparent temperature (green curve) with the real temperature of the shock front (purple curve) is shown in Fig. 10. Due to the increasing temperature profile behind the shock front and the increasing optical depth below 450 GPa, the shock-front temperature is overestimated, leading to a flattening of the excursion slope. This model suggests that the real temperature excursion will have a steeper slope than shown by the simulated measurement (green curve) in Fig. 10a, and the B1 Hugoniot will be steeper than observed.

In the study of McWilliams *et al.* (9) the optical depth of shocked-MgO was taken as ~1-μm (or smaller) for pressures above 300 GPa. For those experiments, and due to strong pressure and temperature gradients behind the shock front, a large optical depth will give rise to an overestimation of shock front temperature (9), which will diminish as a function of increasing pressure. Similarly, we expect our *P-T* data presented in Fig. 7 to have a steeper slope between points A and B than was measured, due to the effects described above. However, applying these corrections to shock decay data is complex. Constructing release isentropes from the experimentally-determined Hugoniot requires knowledge of crystal structure and the precise locations of phase boundaries. Calculating the precise optical depth correction for experimental data is beyond the scope of this study.

V. Conclusions

We present an experimental study of Hugoniot pressure-temperature-density states of single-crystal MgO [100] up to 1500 GPa. Our decaying shock data reproduces the temperature excursion observed by previous shock experiments (9, 36). We show that a large optical depth leads to an overestimate of temperature in decaying shock experiments because the SOP collects thermal emission from higher temperature regions behind the shock front. In both this study and previous studies (9, 36), experimental observations diverge from theoretical expectations. This discrepancy suggests that the kinetics of phase transitions and/or crystal orientation dependent deformation (57) may significantly shape the response of materials under high-pressure, high-temperature conditions.

Supplementary Materials

Supplementary Materials provides additional information on the target assembly, and methods employed for impedance matching, velocimetry, and pyrometry. There is also additional information on the model employed to account of the optical depth corrections to simulated pressure-temperature experimental data. There are four figures and two data tables.

[1] D. Valencia, R. J. O'Connell, and D. Sasselov, "Internal structure of massive terrestrial planets," *Icarus*, vol. 181, pp. 545–554, 2006.
[2] F. Birch, "Elasticity and constitution of the Earth's interior," *J. Geophys. Res.*, vol. 57, no. 2, pp. 227–286, 1952.
[3] A. E. Ringwood, "Phase transformations and their bearing on the constitution and dynamics of the mantle," *Geochimica et Cosmochimica Acta*, vol. 55, no. 8, pp. 2083–2110, 1991.
[4] A. Zerr and R. Boehler, "Constraints on the melting temperature of the lower mantle from high-pressure experiments on MgO and magnesioüstite," *Nature*, vol. 371, pp. 506–508, 1994.
[5] T. S. Duffy, R. J. Hemley, and H. K. Mao, "Equation of state and shear strength at multimegabar pressures: Magnesium oxide to 227 GPa," *Physical Review Letters*, vol. 74, no. 8, pp. 1371–1374, 1995.

[6] N. de Koker and L. Stixrude, "Self-consistent thermodynamic description of silicate liquids, with application to shock melting of MgO periclase and $MgSiO_3$ perovskite," *Geophys. J. Int.*, vol. 178, 2009.

[7] F. Coppari, R. F. Smith, J. H. Eggert, J. Wang, J. R. Rygg, A. Lazicki, J. A. Hawreliak, G. W. Collins, and T. S. Duffy, "Experimental evidence for a phase transition in magnesium oxide at exoplanet pressures," *Nat. Geosci.*, vol. 6, no. 11, pp. 926–929, 2013.

[8] J. K. Wicks, S. Singh, M. Millot, D. E. Fratanduono, F. Coppari, M. Gorman, Z. Ye, J. R. Rygg, A. Hari, J. H. Eggert, T. S. Duffy, and R. F. Smith, "B1-B2 transition in shock-compressed MgO," *Science Advances*, vol. 10, no. 23, p. eadk0306, 2024.

[9] R. S. McWilliams, D. K. Spaulding, J. H. Eggert, P. M. Celliers, D. G. Hicks, R. F. Smith, G. W. Collins, and R. Jeanloz, "Phase transformations and metallization of magnesium oxide at high pressure and temperature," *Science*, vol. 338, no. 6112, pp. 1330–1333, 2012.

[10] S. Root, L. Shulenburger, R. W. Lemke, D. H. Dolan, T. R. Mattsson, and M. P. Desjarlais, "Shock Response and Phase Transitions of MgO at Planetary Impact Conditions," *Phys. Rev. Lett.*, vol. 115, no. 19, pp. 1–6, 2015.

[11] J. Bouchet, F. Bottin, V. Recoules, F. Remus, G. Morard, R. M. Bolis, and A. Benuzzi-Mounaix, "Ab initio calculations of the B1-B2 phase transition in MgO," *Physical Reknudson B*, vol. 99, no. 9, pp. 1–10, 2019.

[12] F. Soubiran and B. Militzer, "Anharmonicity and phase diagram of magnesium oxide in the megabar regime," *Phys. Rev. Lett.*, vol. 125, no. 17, pp. 1–6, 2020.

[13] S. ichiro Karato, "Rheological structure of the mantle of a super-Earth: Some insights from mineral physics," *Icarus*, vol. 212, no. 1, pp. 14–23, 2011.

[14] S. Ritterbex, T. Harada, and T. Tsuchiya, "Vacancies in MgO at ultrahigh pressure: About mantle rheology of super-Earths," *Icarus*, vol. 305, pp. 350–357, 2018.

[15] F. Soubiran and B. Militzer, "Electrical conductivity and magnetic dynamos in magma oceans of Super-Earths," *Nature Communications*, vol. 9, no. 1, 2018.

[16] K. Miyanishi, Y. Tange, N. Ozaki, T. Kimura, T. Sano, Y. Sakawa, T. Tsuchiya, and R. Kodama, "Laser-shock compression of magnesium oxide in the warm-dense-matter regime," *Physical Review E - Statistical, Nonlinear, and Soft Matter Physics*, vol. 92, no. 2, pp. 1–5, 2015.

[17] B. Boates and S. A. Bonev, "Demixing instability in dense molten $MgSiO_3$ and the phase diagram of MgO," *Physical Review Letters*, vol. 110, no. 13, pp. 1–5, 2013.

[18] A. B. Belonoshko, S. Arapan, R. Martonak, and A. Rosengren, "MgO phase diagram from first principles in a wide pressure-temperature range," *Phys. Rev. B*, vol. 81, no. 5, p. 054110, 2010.

[19] A. R. Oganov and P. I. Dorogokupets, "All-electron and pseudopotential study of MgO: Equation of state, anharmonicity, and stability," *Phys. Rev. B*, vol. 67, no. 22, p. 224110, 2003.

[20] Z. Wu, R. M. Wentzcovitch, K. Umemoto, B. Li, K. Hirose, and J.-C. Zheng, "Pressure-volume-temperature relations in MgO: An ultrahigh pressure-temperature scale for planetary sciences applications," *J. Geophys. Res.*, vol. 113, no. B6, 2008.

[21] H. Abu-Farsakh, I. Al-Qasir, and A. Qteish, "Fundamental properties and phase stability of B1 and B2 phases of MgO over a wide range of pressures and temperatures: A first-principles study," *Comput. Mater. Sci*, vol. 154, pp. 159–168, 2018.

[22] R. Musella, S. Mazevet, and F. Guyot, "Physical properties of MgO at deep planetary conditions," *Phys. Rev. B*, vol. 99, no. 6, p. 064110, 2019.

[23] S. Zhang, R. Paul, S. Hu, and M. A. Morales, "Toward an accurate equation of state and B1-B2 phase boundary for magnesium oxide up to terapascal pressures and electron-volt temperatures," *Physical Review B*, vol. 107, no. 22, p. 224109, 2023.

[24] H. Abu-Farsakh, I. Al-Qasir, and A. Qteish, "Fundamental properties and phase stability of B1 and B2 phases of MgO over a wide range of pressures and temperatures: A first-principles study," *Computational Materials Science*, vol. 154, no. July, pp. 159–168, 2018.

[25] S. P. Lyon and J. D. Johnson, "Sesame: the Los Alamos National Laboratory equation of state database," *Los Alamos National Laboratory, Los Alamos, NM, LA-UR-92-3407*, 1992.

[26] M. Millot, N. Dubrovinskaia, A. Černok, S. Blaha, L. Dubrovinsky, D. G. Braun, P. M. Celliers, G. W. Collins, J. H. Eggert, and R. Jeanloz, "Shock compression of stishovite and melting of silica at planetary interior conditions," *Science*, vol. 347, no. 6220, pp. 418–420, 2015.

[27] M. Millot, S. Zhang, D. E. Fratanduono, F. Coppari, S. Hamel, B. Militzer, D. Simonova, S. Shcheka, N. Dubrovinskaia, L. Dubrovinsky, *et al.*, "Recreating giants impacts in the laboratory: Shock compression of bridgmanite to 14 Mbar," *Geophysical Research Letters*, vol. 47, no. 4, p. e2019GL085476, 2020.

[28] J. T. Larsen and S. M. Lane, "HYADES—A plasma hydrodynamics code for dense plasma studies," *J. Quant. Spectrosc. Ra.*, vol. 51, no. 1, pp. 179–186, 1994.

[29] P. M. Celliers, D. K. Bradley, G. W. Collins, D. G. Hicks, T. R. Boehly, and W. J. Armstrong, "Line-imaging velocimeter for shock diagnostics at the OMEGA laser facility," *Rev. Sci. Instrum.*, vol. 75, no. 11, p. 4916, 2004.

[30] P. M. Celliers and M. Millot, "Imaging velocity interferometer system for any reflector (VISAR) diagnostics for high energy density sciences," *Review of Scientific Instruments*, vol. 94, 01 2023. 011101.

[31] M. C. Gregor, R. Boni, A. Sorce, J. Kendrick, C. A. McCoy, D. N. Polsin, T. R. Boehly, P. M. Celliers, G. W. Collins, D. E. Fratanduono, J. H. Eggert, and M. Millot, "Absolute calibration of the OMEGA streaked optical pyrometer for temperature measurements of compressed materials," *Review of Scientific Instruments*, vol. 87, no. 11, pp. 1–8, 2016.

[32] Y. B. Zeldovich and Y. P. Raizer, *Physics of shock waves and high-temperature hydrodynamic phenomena*. Courier Corporation, 2002.

[33] M. Millot, "Identifying and discriminating phase transitions along decaying shocks with line imaging doppler interferometric velocimetry and streaked optical pyrometry," *Physics of Plasmas*, vol. 23, no. 1, 2016.

[34] P. M. Celliers and M. Millot, "Imaging velocity interferometer system for any reflector (visar) diagnostics for high energy density sciences," *Review of Scientific Instruments*, vol. 94, no. 1, 2023.

[35] D. Hicks, T. Boehly, P. Celliers, J. Eggert, E. Vianello, D. Meyerhofer, and G. Collins, "Shock compression of quartz in the high-pressure fluid regime," *Phys. Plasmas*, vol. 12, no. 8, p. 082702, 2005.

[36] R. M. Bolis, G. Morard, T. Vinci, A. Ravasio, E. Bambrink, M. Guarguaglini, M. Koenig, R. Musella, F. Remus, J. Bouchet, N. Ozaki, K. Miyanishi, T. Sekine, Y. Sakawa, T. Sano, R. Kodama, F. Guyot, and A. Benuzzi-Mounaix, "Decaying shock studies of phase transitions in MgO-SiO_2 systems: Implications for the super-Earths' interiors," *Geophysical Research Letters*, vol. 43, no. 18, pp. 9475–9483, 2016.

[37] D. G. Hicks, T. R. Boehly, J. H. Eggert, J. E. Miller, P. M. Celliers, and G. W. Collins, "Dissociation of liquid silica at high pressures and temperatures," *Physical Review Letters*, vol. 97, no. 2, pp. 3–6, 2006.

[38] J. H. Eggert, D. G. Hicks, P. M. Celliers, D. K. Bradley, R. S. McWilliams, R. Jeanloz, J. E. Miller, T. R. Boehly, and G. W. Collins, "Melting temperature of diamond at ultrahigh pressure," *Nature Physics*, vol. 6, no. 1, pp. 40–43, 2010.

[39] A. Olivier, D. G. Giovanis, B. Aakash, M. Chauhan, L. Vandanapu, and M. D. Shields, "Uqpy: A general purpose python package and development environment for uncertainty quantification," *Journal of Computational Science*, vol. 47, p. 101204, 2020.

[40] D. E. Fratanduono, T. R. Boehly, P. M. Celliers, M. A. Barrios, J. H. Eggert, R. F. Smith, D. G. Hicks, G. W. Collins, and D. D. Meyerhofer, "The direct measurement of ablation pressure driven by 351-nm laser radiation," *J. Appl. Phys.*, vol. 110, no. 7, p. 073110, 2011.

[41] M. Millot, P. A. Sterne, J. H. Eggert, S. Hamel, M. C. Marshall, and P. M. Celliers, "High-precision shock equation of state measurements for metallic fluid carbon between 15 and 20 Mbar," *Physics of Plasmas*, vol. 27, no. 10, 2020.

[42] Y.-J. Kim, B. Militzer, B. Boates, S. Bonev, P. M. Celliers, G. W. Collins, K. P. Driver, D. E. Fratanduono, S. Hamel, R. Jeanloz, J. R. Rygg, D. C. Swift, J. H. Eggert, and M. Millot, "Evidence for Dissociation and Ionization in Shock Compressed Nitrogen to 800 GPa," *Phys. Rev. Lett.*, vol. 129, p. 015701, Jun 2022.

[43] D. G. Hicks, T. R. Boehly, P. M. Celliers, D. K. Bradley, J. H. Eggert, R. S. McWilliams, R. Jeanloz, and G. W. Collins, "High-precision measurements of the diamond Hugoniot in and above the melt region," *Physical Review B - Condensed Matter and Materials Physics*, vol. 78, no. 17, pp. 1–8, 2008.

[44] M. D. Knudson and M. P. Desjarlais, "Adiabatic release measurements in α-quartz between 300 and 1200 GPa: Characterization of α-quartz as a shock standard in the multimegabar regime," *Physical Review B - Condensed Matter and Materials Physics*, vol. 88, no. 18, 2013.

[45] S. Brygoo, M. Millot, P. Loubeyre, A. E. Lazicki, S. Hamel, T. Qi, P. M. Celliers, F. Coppari, J. H. Eggert, D. E. Fratanduono, *et al.*, "Analysis of laser shock experiments on precompressed samples using a quartz reference and application to warm dense hydrogen and helium," *Journal of Applied Physics*, vol. 118, no. 19, p. 195901, 2015.

[46] A. Fernandez-Pañella, M. Millot, D. Fratanduono, M. Desjarlais, S. Hamel, M. Marshall, D. Erskine, P. Sterne, S. Haan, T. Boehly, *et al.*, "Shock compression of liquid deuterium up to 1 TPa," *Physical Review Letters*, vol. 122, no. 25, p. 255702, 2019.

[47] C. A. McCoy, M. C. Marshall, D. N. Polsin, D. E. Fratanduono, P. M. Celliers, D. D. Meyerhofer, and T. R. Boehly, "Hugoniot, sound velocity, and shock temperature of MgO to 2300 GPa," *Phys. Rev. B*, vol. 100, p. 014106, Jul 2019.

[48] S. P. Marsh, *LASL Shock Hugoniot Data*. Univ of California Press, 1980.

[49] J. Wu, F. González-Cataldo, F. Soubiran, and B. Militzer, "The phase diagrams of beryllium and magnesium oxide at megabar pressures," *Journal of Physics Condensed Matter*, vol. 34, no. 14, 2022.

[50] D. E. Fratanduono, J. H. Eggert, M. C. Akin, R. Chau, and N. C. Holmes, "A novel approach to Hugoniot measurements utilizing transparent crystals," *Journal of Applied Physics*, vol. 114, no. 4, p. 043518, 2013.

[51] G. R. Fowles, "Shock wave compression of hardened and annealed 2024 aluminum," *J. Appl. Phys.*, vol. 32, no. 8, p. 1475, 1961.

[52] R. Hill, "The mathematical theory of plasticity," *Oxford University Press, New York*, 1950.

[53] Z. Ye, R. F. Smith, S. Singh, M. Millot, D. E. Fratanduono, F. Coppari, and J. K. Wicks, "Experimental evidence for orientation-dependent phase transitions under shock compression," in preparation, 2024.

[54] D. Cebulla and R. Redmer, "Ab initio simulations of MgO under extreme conditions," *Physical Review B - Condensed Matter and Materials Physics*, vol. 89, no. 13, pp. 1–10, 2014.

[55] Q. Liu, T. Xue, J. Li, J. Li, and X. Zhou, "Optical absorption spectra of MgO single crystals under shock compression between 50 and 132 GPa," *Journal of Applied Physics*, vol. 131, no. 23, 2022.

[56] I. Yonenaga, Y. Ohno, T. Taishi, Y. Tokumoto, H. Makino, T. Yao, Y. Kamimura, and K. Edagawa, "Optical properties of fresh dislocations in GaN," *Journal of crystal growth*, vol. 318, no. 1, pp. 415–417, 2011.

[57] P. Renganathan and Y. Gupta, "Melting anisotropy in crystalline solids," *Physical Review B*, vol. 109, no. 6, p. L060102, 2024.

[58] D. J. Erskine, J. Eggert, P. Celliers, and D. Hicks, "Ghost fringe removal techniques using lissajous data presentation," *Review of Scientific Instruments*, vol. 87, no. 3, 2016.

[59] L. Zhang and Y. Fei, "Melting behavior of (Mg, Fe)O solid solutions at high pressure," *Geophys. Res. Lett.*, vol. 35, no. 13, p. L13302, 2008.

[60] M. S. Vassiliou and T. J. Ahrens, "Hugoniot equation of state of periclase to 200 GPa," *Geophysical Research Letters*, vol. 8, no. 7, pp. 729–732, 1981.

[61] T. S. Duffy, "Mineralogy at the extremes," *Nature*, vol. 451, no. 7176, pp. 269–270, 2008.

[62] I. Jackson and H. Niesler, "The elasticity of periclase to 3 GPa and some geophysical implications," *High Pressure Research in Geophysics*, pp. 93–113, 1982.

[63] Q. Liu, T. Xue, J. Li, J. Li, and X. Zhou, "Optical absorption spectra of MgO single crystals under shock compression between 50 and 132 GPa," *Journal of Applied Physics*, vol. 131, no. 23, 2022.

[64] Y. Luo, S. Xiang, J. Li, J. Wu, L. Liu, J. Li, Y. Xian, and R. Wu, "Equation of state of MgO up to 345 GPa and 8500 K," *Physical Review B*, vol. 107, no. 13, pp. 16–18, 2023.

[65] M. Millot, S. Hamel, J. R. Rygg, P. M. Celliers, G. W. Collins, F. Coppari, D. E. Fratanduono, R. Jeanloz, D. C. Swift, and J. H. Eggert, "Experimental evidence for superionic water ice using shock compression," *Nature Physics*, vol. 14, no. 3, pp. 297–302, 2018.

Acknowledgements: This work was supported by the U.S. Department of Energy through the National Laser Users' Facility Program (NLUF) under Contract No. DE-NA0003933 awarded to Principal Investigator Wicks through Johns Hopkins University. Part of this work was performed under the auspices of the U.S. Department of Energy by the Lawrence Livermore National Laboratory under Contract No. DE-AC52-07NA27344 and the Laboratory Directed Research and Development Program at LLNL (project no.'s 15-ERD-014, 17-ERD-014, 20-ERD-044). A portion of this work was sponsored by the Department of the Defense, Defense Threat Reduction Agency under the MSEE URA, HDTRA1-20-2-0001. The content of the information does not necessarily reflect the position or the policy of the federal government, and no official endorsement should be inferred. The experiments were conducted at the Omega Laser Facility at the University of Rochester's Laboratory for Laser Energetics. We thank the Omega-EP Laser operations staff and the Target Engineering Team at Lawrence Livermore National Laboratory (LLNL) for assistance in these experiments. We thank François Soubiran for helpful discussions. Zixuan Ye Summer Internship at LLNL was supported by the High Energy Density Science Center. The LLNL AnalyzeVISAR code was used to analyze the data.